Petroleum Science 23 (2026) 2808–2820

Contents lists available at ScienceDirect

Petroleum Science

journal homepage: www.keaipublishing.com/en/journals/petroleum-science

Original Paper

Experimental study of the flow characteristics of surfactant-assisted aerosols in low permeability porous media

Ping Jiang [a,b,*], Chen-Xi Li [a,b], Kai Guo [a,b], Gui-Cai Zhang [a,b], Ji-Jiang Ge [a,b], Ning Qi [a,b], Yu-Kun Lu [c]

[a] Key Laboratory of Unconventional Oil & Gas Development (China University of Petroleum (East China)), Ministry of Education, Qingdao, 266580, Shandong, China
[b] School of Petroleum Engineering, China University of Petroleum (East China), Qingdao, 266580, Shandong, China
[c] School of Chemistry and Chemical Engineering and State Key Laboratory of Heavy Oil Processing, China University of Petroleum (East China), Qingdao, 266580, Shandong, China

ARTICLE INFO

Article history:
Received 25 June 2025
Received in revised form
14 January 2026
Accepted 15 January 2026
Available online 19 January 2026

Edited by Yan-Hua Sun

Keywords:
Aerosol
Gas flooding
Gas channeling
CO_2 geo-storage
Interface modulus

ABSTRACT

Gas channeling in formations is a primary factor affecting the effectiveness of gas flooding and CO_2 geo-storage. Current dominant methods for controlling gas channeling include water-alternating-gas injection and foam flooding, among others. This study proposes an innovative approach using an aerosol system to manage gas channeling in low-permeability reservoirs. Through ANSYS simulation, an effervescent aerosol generator was selected and optimized. Two surfactants, sodium dodecyl sulfate and polyoxyethylene (20) cetyl ether, were employed to assist aerosol generation. Core flooding experiments were conducted to investigate the flow characteristics of aerosols in porous media and revealed that the liquid phase content significantly influenced flow pressure. For instance, in a water aerosol system with a total mass flow rate of 5.5 mg/s, increasing the liquid–gas flow ratio from 0.2 to 0.8 resulted in an approximately 53% rise in balance pressure and an 185% increase in the resistance factor. Nuclear magnetic resonance scanning was used to examine aerosol distribution patterns with and without surfactants. In water aerosol injections, aerosols preferentially occupied pores with radii of 0.16–0.83 μm, whereas surfactant-assisted aerosols predominantly entered pores with radii of 0.04–0.21 μm, indicating that the addition of surfactants enhances injectability and blocking capacity.

1. Introduction

Introducing CO_2 into reservoirs has proven to be an efficient method to enhance oil recovery (EOR) while simultaneously allowing for the geo-storage of CO_2 (Zhang et al., 2024). However, when CO_2 is injected alone, gas channeling and viscous fingering frequently occur, thereby negatively impacting both enhanced oil recovery and geo-storage.

At present, the application of mature methods for the prevention of gas channeling includes water-alternating-gas (WAG) injection and foam flooding (Chen et al., 2024; Khan et al., 2016; Roozbahani et al., 2024; Sun et al., 2021; Wang et al., 2023; Wang et al., 2017). Both methods have been shown to reduce gas permeability by lowering gas saturation within the flow channel and utilizing capillary forces at the gas–liquid interface (Ren and Duncan, 2021; Yan et al., 2017). The concept of WAG technology was initially proposed in the 1960s and has since been extensively implemented (Kumar and Mandal, 2017). Several elements influence the success of WAG injection in averting gas channeling, such as the gas's composition (Wang et al., 2021), the ratio of water to gas (Vivek et al., 2017), the water phase's salinity (Chaturvedi et al., 2021), the reservoir's heterogeneity (Spiteri and Juanes, 2006), the tension and interfacial viscoelasticity at gas–liquid interface, along with the initial viscosity of the crude oil in the subsurface and CO_2's role in reducing viscosity (Abdurrahman et al., 2021). In typical WAG implementation, the gas–water ratio is often set at 1. However, some studies suggest that the optimal gas–water ratio for actual reservoirs ranges from 0.6 to 0.8. This ratio exceeds the values observed in core tests and those typically employed in most conventional oil fields. The underlying reason for this phenomenon

* Corresponding author.
E-mail address: jiangping@upc.edu.cn (P. Jiang).
Peer review under the responsibility of China University of Petroleum (Beijing).

https://doi.org/10.1016/j.petsci.2026.01.021

is attributable to the heterogeneity of the reservoirs, which enables the migration of gas through the reservoirs (Wei et al., 2021). The addition of surfactants to WAG has been demonstrated to promote foam formation and reduce interfacial tension, thereby enhancing CO_2 utilization efficiency compared to traditional WAG injection (da Silva et al., 2022). Additionally, foam flooding is also a commonly used technique for preventing CO_2 gas channeling. Foam can be defined as a dispersed system of gas within a liquid. In comparison with CO_2, foam demonstrates increased viscosity and the capacity to reduce gas permeability through the Jamin effect, thereby enhancing volumetric sweep efficiency (Simjoo et al., 2013).

Nevertheless, both WAG and foam flooding face numerous challenges in practical applications. Firstly, in low-permeability reservoirs, high injection pressures or even difficulties in water injections arise, resulting in the poor effectiveness of WAG and foam flooding in such formations (Rostami et al., 2026). Secondly, the massive injection of fluids into reservoirs can cause swelling of clay minerals within the rock, damaging the reservoir (Cho et al., 2021). Finally, the compressibility of gas renders the control of the gas–liquid ratio a challenging task, a problem that is particularly severe in the context of foam flooding. Consequently, controlling gas channeling while reducing the water phase content in the injection system remains a critical challenge in CO_2 flooding technology.

Aerosols can be defined as relatively stable polydisperse systems formed by liquid or solid particles suspended in a gas (Kokhanovsky, 2013; Dubovik et al., 2019), with particle sizes ranging from 0.001 to 100 μm (Pöschl, 2005). It is evident that there is a multitude of natural aerosol systems present within the environment (Choudhury et al., 2019; Lin et al., 2021). Concurrently, anthropogenic activities result in the generation of diverse types of aerosols, encompassing solid particulate matter produced during combustion processes (Wang et al., 2022). The physical properties of aerosols, including but not limited to particle shape, concentration, and size distribution, significantly influence their dynamics and stability. For liquid particle aerosols, the interaction between particle concentration and particle size distribution has been shown to collectively influence aerosol condensation and deposition (Hinds and Zhu, 2022). The condensation rate is directly proportional to the square of the particle concentration. It has been demonstrated that higher concentrations have a direct impact on the rate of particle collisions and the process of condensation. This, in turn, results in a consequential alteration to the size distribution. In the case of particles of minimal size, intense Brownian motion facilitates collisions. As the particle size increases, Brownian motion weakens, reducing collisions. However, further increases in particle size have been shown to enhance inertia, thereby rendering particles less responsive to airflow turns and more prone to collisions. Furthermore, the particle shape also influences aerosol settling (Lv and Zhao, 2022). It is evident that non-spherical particles characteristically manifest augmented drag and diminished settling velocities in comparison to their spherical counterparts of equivalent volume. However, due to the presence of surface tension, liquid particles generally assume a spherical shape.

Traditional aerosol preparation techniques include impinging atomization, pressure atomization, and twin-fluid atomization (O'Sullivan et al., 2019). Impinging atomizers are simple in structure and inexpensive, but they generate aerosols with larger particle sizes and uneven distributions. Pressure atomization produces smaller droplets with narrower distributions; however, it is highly sensitive to liquid viscosity and requires higher pressures to generate fine droplets. The employment of twin-fluid atomization facilitates the attainment of precise control over a range of parameters, including droplet size distribution, atomization cone angle, spray momentum, and flow rate. However, the complex structure necessitates the implementation of two sets of pipelines, resulting in increased costs and substantial gas consumption. In addition to the three conventional aerosol preparation techniques outlined above, alternative methods have been proposed (Zhao et al., 2025; Lwin et al., 2020). The effervescent atomization technology developed in the late 1980s has gained widespread application due to its advantageous properties, including low gas flow requirements, strong adaptability, insensitivity to viscosity, and simple structure (Ochowiak et al., 2018). The principle behind this process involves the simultaneous injection and mixing of gas and liquid to form a stable bubble flow that is ejected from the outlet. Upon ejection, the bubble undergoes rapid expansion, collision, and rupture due to the drastic change in pressure difference between its interior and exterior. The process entails the fragmentation of the liquid phase into tiny droplets, which are then dispersed into the gas (Sun et al., 2018).

The Jamin effect, generated by the interaction of droplets and gas within aerosols, can regulate gas flow and control gas channeling. A comparison of aerosol systems with WAG and foam flooding reveals that the former can achieve lower water content and higher gas content. In recent years, a significant number of scholars have investigated the phenomenon of aerosol flow in porous media. However, most of these studies have focused on the transport of aerosols in soil (Hall et al., 2016; Chen et al., 2022). Moreover, the application of aerosols in petroleum development remains largely unexplored. Wang et al. (2025) reported a novel CO_2 aerosol foam system (CAFS). In comparison with conventional CO_2 foam systems (CF), CAFS enhances foam uniformity and stability through the incorporation of aerosol, thereby increasing recovery rates by 10.45%.

In this paper, we utilized ANSYS to design and optimize the structure of an effervescent aerosol generator. The objective of this study was to undertake an investigation into the effects of injection parameters and interfacial properties of the aerosol on the regulation of seepage pressure within porous media. To this end, an experimental approach was adopted, involving the injection of aerosol into rock cores. Moreover, nuclear magnetic resonance analysis methods were employed to characterize the influence of water saturation on seepage resistance. The conclusions drawn from this work contribute to understanding the flow characteristics of aerosols in porous media and provide insights for their application in petroleum development and carbon storage.

2. Materials and methods

2.1. Materials

Ammonium chloride (NH_4Cl) and anionic surfactant sodium dodecyl sulfate (SDS) were purchased from Sinopharm Chemical Reagent, Shanghai, China. Nonionic surfactant polyoxyethylene (20) cetyl ether ($C_{16}E_{20}$) was purchased from Sigma Aldrich, Shanghai, China. Methanol was purchased from Merck, Germany. Distilled water was homemade using YL-100BU laboratory ultrapure water machine. The gas used in the experiment was 99.9% pure CO_2, purchased from Qingdao Tianyuan Gas Manufacturing Co.

Importantly, to inhibit the entry of the aqueous phase into the core, which causes clay swelling and alters the pore structure of the core, all experimental aqueous phases contained a 0.748 mol/L NH_4Cl solution. All other systems containing surfactants were prepared using this liquid phase.

2.2. Surface tension and interface modulus measurements

Surface tension and interfacial modulus were measured using the droplet profile analyzer DSA100 with droplet oscillation module via small-amplitude low-frequency oscillations. The

surface tension was determined by immersing a stainless-steel capillary tube in a quartz cuvette filled with CO_2 and extruding an aqueous-phase droplet of a specified size at the tip of the capillary tube using an injection system. Subsequently, the droplet surface area was modified in sinusoidal signal mode (frequency is 0.1 Hz) via the droplet oscillation module, and the corresponding dynamic surface tension was quantified and documented by the software provided with the instrument. The recorded data were processed using the instrument's built-in data analysis software, which automatically calculated the corresponding interfacial modulus. During the oscillation process, the rate of change of the droplet interfacial area was maintained at 2%, and the experiment was conducted at room temperature.

2.3. Aerosol generator models and simulation methods

ANSYS simulation software was employed to complete the modelling and structural optimization of the aerosol generator. The design of the aerosol generator model was accomplished through the utilization of SpaceClaim module, which facilitated the simplification of the 3D model and the extraction of the fluid domain. Subsequently, mesh generation was conducted in Mesh module. The meshed model was imported into Fluent module for simulation. The multiphase flow model employed the Eulerian model, with CO_2 designated as the primary phase and water as the secondary phase. The standard k–ε model was selected as the turbulence model. The inlets were configured as mass flow inlets, and the outlet as a pressure outlet. The solver method that was selected was the Coupled algorithm. The pressure term equation selected was PRESTO!, while all other equations employed first order upwind schemes.

Jiangsu Haian Petroleum Technology Instrument Co., Ltd. was commissioned to manufacture the aerosol generator based on the optimized structural diagram.

2.4. Core flooding experiments

(1) Pre-treatment: The experiments were conducted using Berre sandstone cores (cylindrical, 10±0.08 cm long, 2.5±0.02 cm in diameter). To eliminate any salt contamination, the cores were meticulously washed in a Soxhlet setup under reflux conditions with methanol for 2 d before each experiment. After washing, the cores were heated at 100 °C in an oven for 12 h, then cooled and set aside for later use.

(2) Parameter settings: The core was inserted into the core holder, and the incubator temperature was set to 40 °C. The confining pressure of the core holder was set to 6 MPa. It was ensured that the confining pressure exceeded the inlet pressure by at least 3 MPa to close the gap between the core and the core holder. Simultaneously, a back pressure of 1 MPa was applied at the outlet of the core holder. All subsequent pressure data represents pressure values after subtracting back pressure.

(3) Flooding experiments: The CO_2 cylinder was opened, and the flow rate was adjusted to the desired value using the flow controller. CO_2 was then injected into the core till the pressure stabilized, and the initial permeability k_1 of the core was calculated based on the pressure. Subsequently, the pump was activated, and the liquid flow rate was adjusted to ensure thorough mixing of water and CO_2 within the aerosol generator. The resulting aerosol was injected into the core until the pressure gradually stabilized. At this point, the aerosol permeability k_2 was calculated based on the average pressure value.

(4) Post-processing: To prevent NH_4Cl and surfactants from accumulating in the pores and interfering with the experiment, the core was cleaned again following the procedure described in Step (1).

The experimental setup is depicted in Fig. 1.

According to Darcy's law

$$k_g = \frac{2Q_0 p_0 \mu L}{A(p_1^2 - p_2^2)} \tag{1}$$

where k_g is the gas permeability; p_1 is the inlet pressure; p_2 is the outlet pressure; p_0 is the atmospheric pressure; μ is the gas viscosity; Q_0 is the volumetric flow rate of the gas at p_0; A is the cross-sectional area of the core; and L is the length of the core.

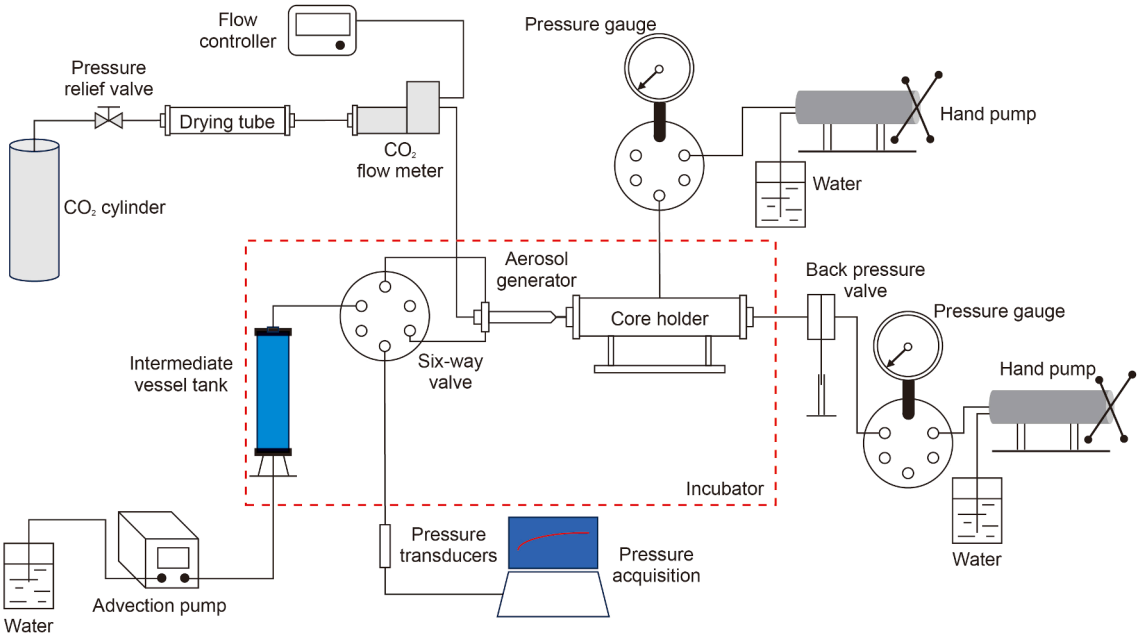

Fig. 1. Schematic illustration of core flooding set-up.

The initial permeability k_1 and aerosol permeability k_2 can be obtained from Eq. (1). The drag factor is defined as the ratio of the permeability calculated when CO_2 and aerosols flooding are utilized during the experiments, and its can be deduced from Eq. (1) with the following results:

$$\frac{k_1}{k_2} = \frac{p_{21}^2 - p_{22}^2}{p_{11}^2 - p_{12}^2} \tag{2}$$

where p_{11} and p_{12} are the initial inlet and outlet pressures; while p_{21} and p_{22} are the subsequent inlet and outlet pressures. Considering this research primarily concentrates on the dispersal and movement properties of aerosols in porous materials, the proportion of CO_2 to the aerosols' viscosity in Eq. (2) disregards.

2.5. Nuclear magnetic resonance (NMR) scanning

MacroMR12-150-1, a large-aperture nuclear magnetic resonance imaging analyzer, serves as the experimental tool to examine the variations in the two-phase distribution and saturation of water and gas in the pores at various core scales during aerosols core injection processes.

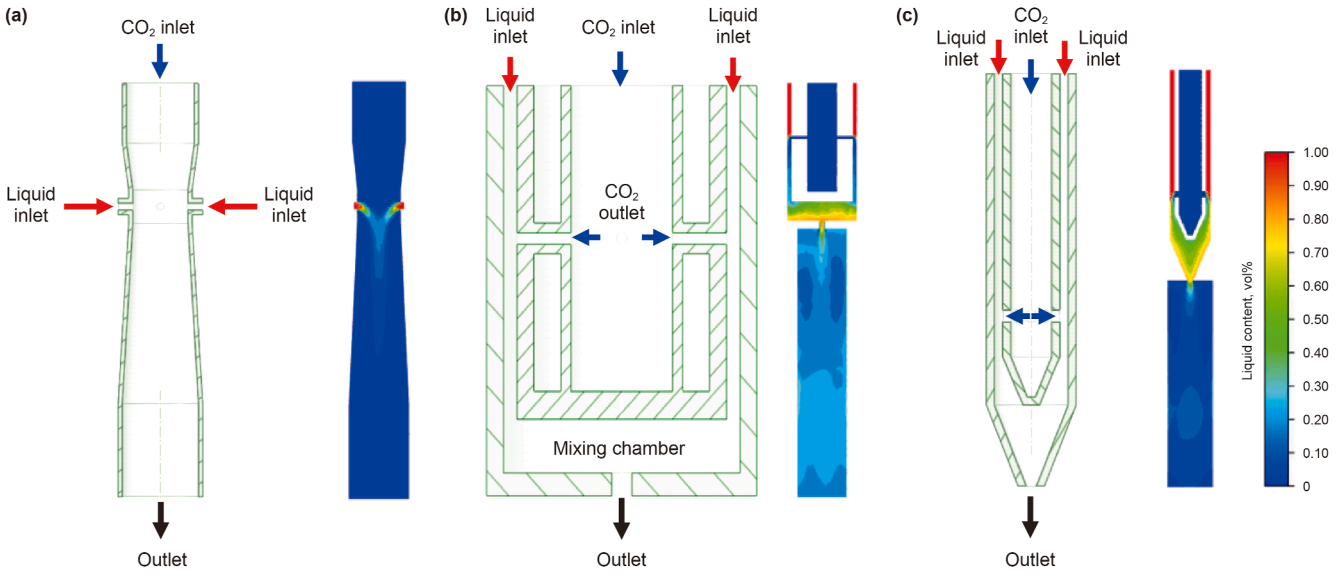

Fig. 2. Cross-sectional views and simulation results of internal mixing twin-fluid aerosol generator (**a**), effervescent generator (**b**), and improved effervescent generator (**c**). Water mass flow rate was 80 g/s, LGR is 100.

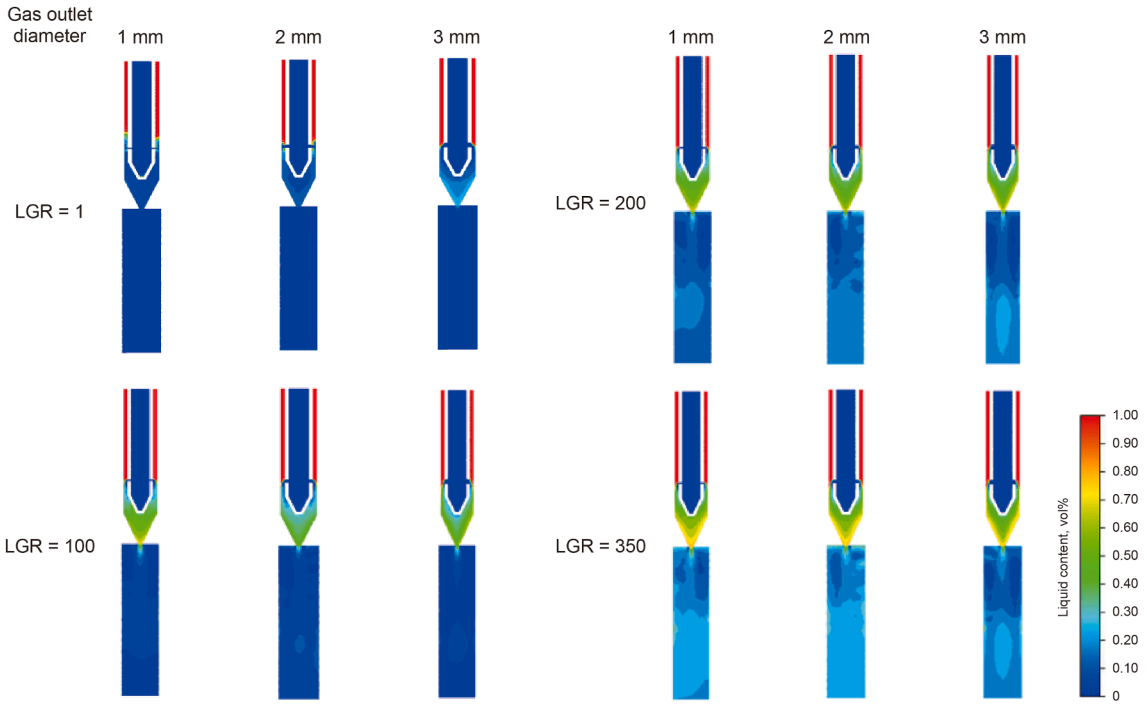

Fig. 3. Simulation results of aerosol generators with different CO_2 outlet diameters.

The core flooding experiments employed NMR. At different intervals after starting, the experiment was temporarily halted. Following the extraction of the core, an NMR scan was conducted. Following this, the core was placed back at the pressure-tapped, and the experiment persisted until it was fully completed.

For the NMR characterization, only the water and $C_{16}E_{20}$ systems were investigated. This is because the anionic surfactant SDS is known to adsorb easily onto sandstone surfaces, which could complicate the interpretation of the phase distribution patterns.

3. Results and discussion

3.1. Structural design and parameter optimization of the aerosol generator

3.1.1. Type selection

Among the various aerosol preparation methods, gas-assisted atomization is the most used. This category encompasses twin-fluid methods and effervescent methods. The twin-fluid method includes internal and external mixing. The external mixing approach fails to converge during computational modeling because the gas and liquid share a common inlet. The design of the internal mixing twin-fluid aerosol generator is outlined in Fig. 2(a). This device utilizes a Venturi tube structure. The chosen cross-section is a longitudinal section through the centerline (as below). The total length of the model is 176 mm. The CO_2 inlet and outlet diameters are 32 and 36 mm, respectively, while the liquid inlet diameter is 3 mm. The four liquid inlets are spaced at 90° intervals. Meanwhile, based on studies by Broniarz-Press et al. (2010) on effervescent atomization, an effervescent aerosol generator was modeled. Its structural cross-section is illustrated in Fig. 2(b). The model's dimensions are as follows: its length is 50 mm, and its diameter is 35 mm. The CO_2 outlet is 1 mm in diameter, with four outlets positioned at 90° intervals. The diameter of each outlet is 3 mm, and the outer flow region extends 100 mm in length with a diameter of 25 mm. The liquid inlet mass flow rate is fixed at 80 g/s, with the liquid–gas mass flow ratio (LGR) ranging from 1 to 1000.

Fig. 2 shows the results of the simulation at an LGR of 100. Despite the twin-fluid aerosol generator's capacity to enable independent control of CO_2 and liquid inlet flows, its convergence is observed to occur exclusively at specific flow rates within a relatively constrained range. Furthermore, issues such as uneven liquid dispersion result in suboptimal atomization performance. The effervescent aerosol generator demonstrates exceptional convergence properties; however, the cylindrical mixing chamber leads to the accumulation of CO_2 and liquid, which hinders bubble flow generation.

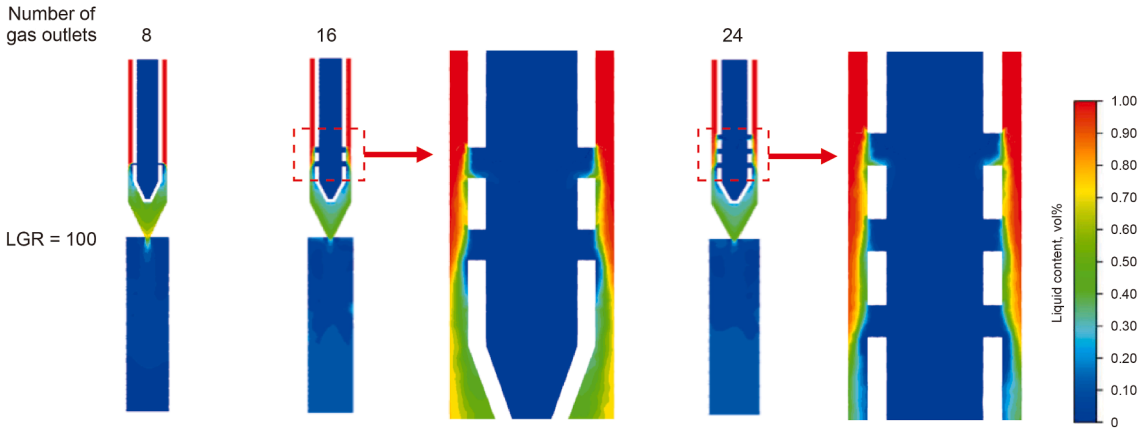

Fig. 4. Simulation results for aerosol generators with different numbers of CO_2 outlets.

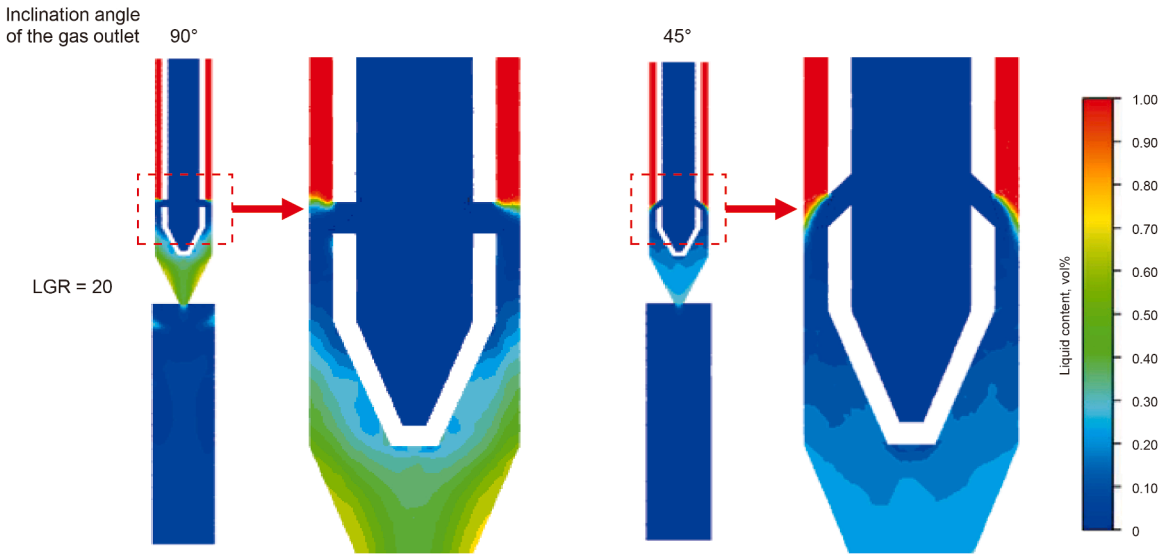

Fig. 5. Simulation results of aerosol generators with different CO_2 outlet angles.

Table 1
Structural parameters of the aerosol generator.

Total length, mm	Wall thickness, mm	Air chamber inner diameter, mm	Liquid chamber inner diameter, mm	Gas outlet diameter, mm	Number of gas outlets	Inclination angle of the gas outlet, °
104	2	14	20	3	8	45

Furthermore, given the impact of relative velocities of CO_2 and liquid outside the CO_2 outlet on liquid shear within the CO_2, the mixing chamber underwent modification from its original cylindrical shape to a tapered design, as illustrated in Fig. 2(c). The number of gas outlets was adjusted to eight, with each outlet measuring 3 mm in diameter. The overall length of the generator is 102 mm, the gas chamber inner diameter is 10 mm, and the wall thickness is uniformly 2 mm. The external diameter of the generator is 22 mm. The simulation results indicate that the improved generator exhibits superior convergence, supports a wider range of LGR, and effectively mitigates the accumulation of gas and liquid phases within the mixing chamber. Consequently, this configuration was chosen for subsequent structural optimization.

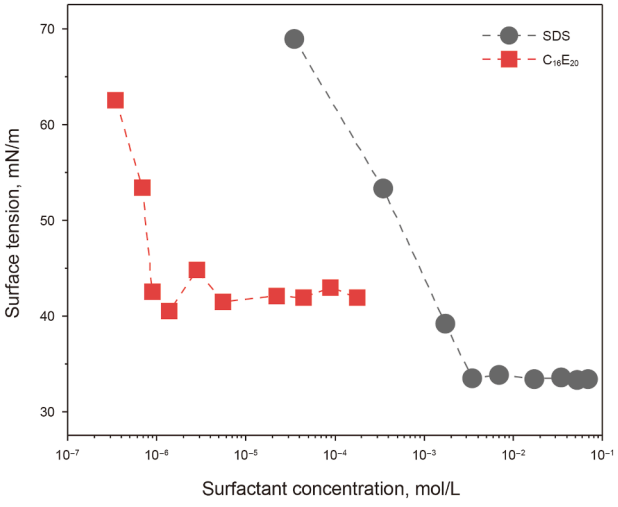

Fig. 6. Surface tension versus surfactant concentration for $C_{16}E_{20}$ and SDS aqueous solutions.

3.1.2. Structural optimization

The location of gas–liquid contact impacts simulation results, so the CO_2 outlets' diameter, number, and distribution pattern were optimized. Initially, the impact of the CO_2 outlet diameter on the flow field within the generator was examined. The outlet diameters were set to 1, 2, and 3 mm. The mass flow rate of water was fixed at 80 g/s, and the CO_2 mass flow rate was adjusted to vary the LGR within the range of 1–1000 (same below). The results are displayed on Fig. 3.

As the flow rate of CO_2 increases, the liquid content within the flow domain gradually decreases. When the LGR drops to 1, water fails to enter the mixing chamber smoothly. The findings of the simulation indicate that for both aerosol generators with outlet diameters of 1 and 2 mm, the liquid phase has difficulty shearing the CO_2 at the outlet. This finding also indicates that aerosol generators with larger outlet diameters offer a broader flow rate adaptability range. Considering the complexity of liquid-phase shearing of the CO_2 and the need to regulate outlet velocity for optimal two-phase mixing, the outlet diameter was set to 3 mm.

The impact of outlet quantity on flow domain in the generator was investigated and the simulation results are shown in Fig. 4. Models with different LGRs show liquid can enter the outlets, which affects aerosol generation. The findings of the simulation comparisons indicate that a single row of outlets is adequate in meeting aerosol preparation requirements. Conversely, excessive outlets have been observed to result in undesirable outcomes, including simulation divergence and suppressed CO_2 flow in the upper outlets. Moreover, an increase in the number of outlets results in a reduction of the flow rate adaptation range.

It has been established that, since the CO_2 encounters the outer water phase at a 90° angle via the outlets, the high relative velocity

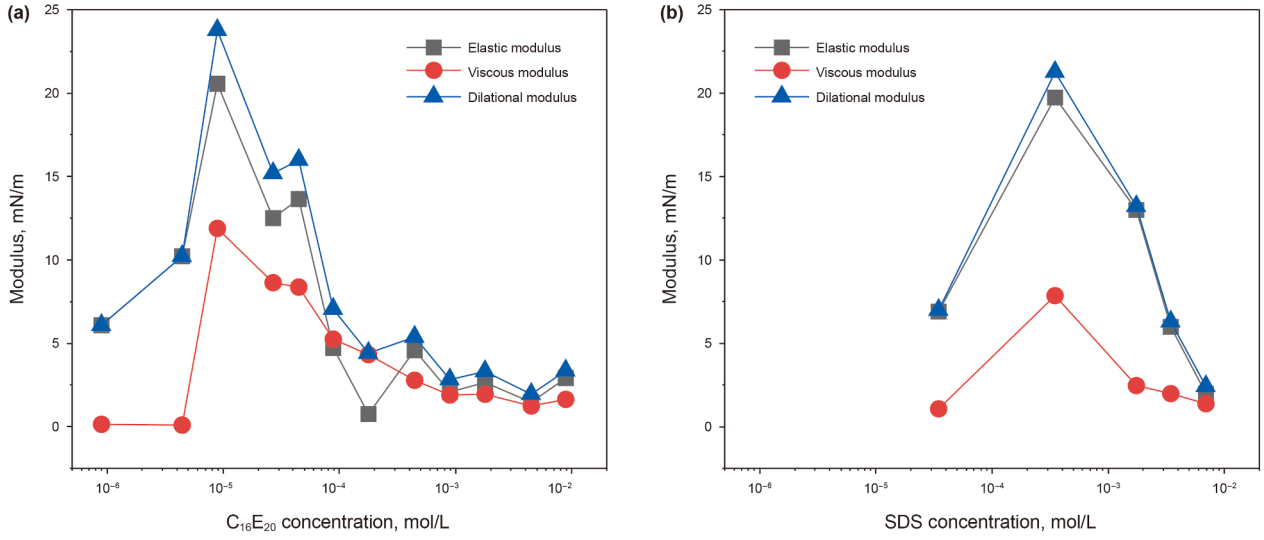

Fig. 7. Viscoelastic parameters (including elastic modulus, viscous modulus, and dilational modulus) versus surfactant concentration for interfaces between gas phase and aqueous solutions containing either $C_{16}E_{20}$ (**a**) or SDS (**b**).

Table 2
Specific information on surfactant systems.

Surfactant	Concentration, mol/L	Surface tension, mN/m	Dilational modulus, mN/m	Elastic modulus, mN/m	Viscous modulus, mN/m
SDS	3.472×10^{-4}	53.27	21.25	19.75	7.84
$C_{16}E_{20}$	8.897×10^{-6}	41.67	23.75	20.57	11.87

between CO_2 and liquid at the outlets also leads to difficulties in liquid shearing the CO_2 and low bubble generation rates. This phenomenon impacts the process of CO_2–liquid mixing within the aerosol generators (Spiteri and Juanes, 2006), necessitating the optimization of the outlet angle design. The outlet angle was modified from perpendicular to the wall surface to a downward inclination of 45°, with the simulation results displayed in Fig. 5.

The simulation results indicate that as the CO_2 inlet mass flow rate gradually increases, the 90° outlet begins to exhibit difficulties

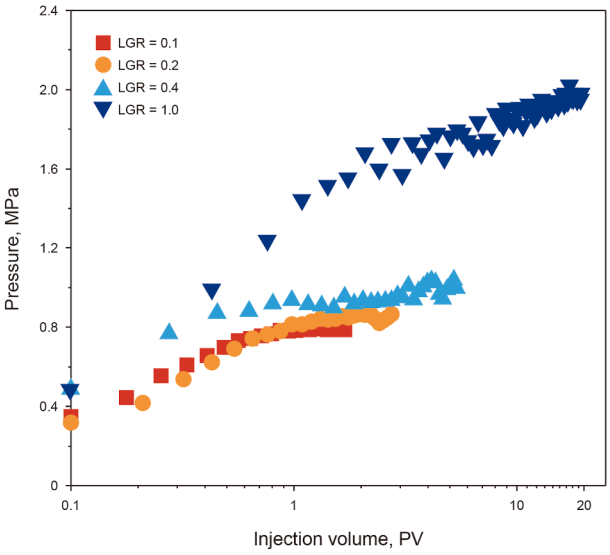

Fig. 8. Curves of injection pressure versus injection volume for water aerosols at different LGRs.

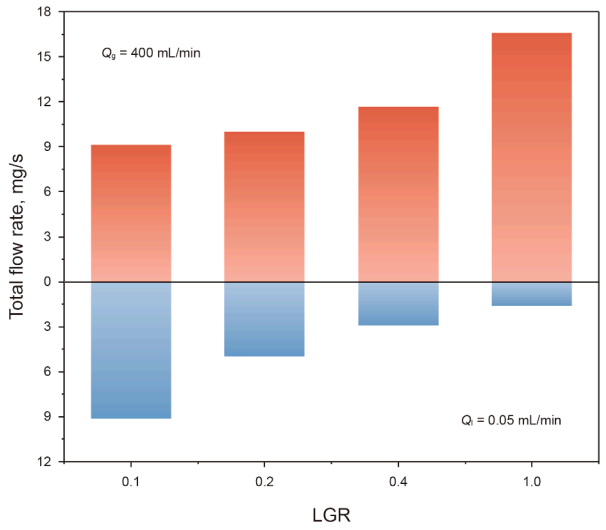

Fig. 10. Total mass flow rate of aerosols under different LGRs.

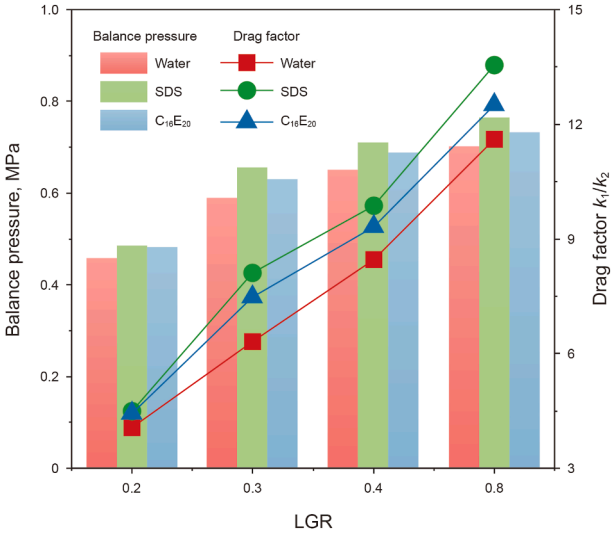

Fig. 11. Effect of varying LGRs on balance pressure and drag factor. Total mass flow rate was fixed at 5.5 mg/s.

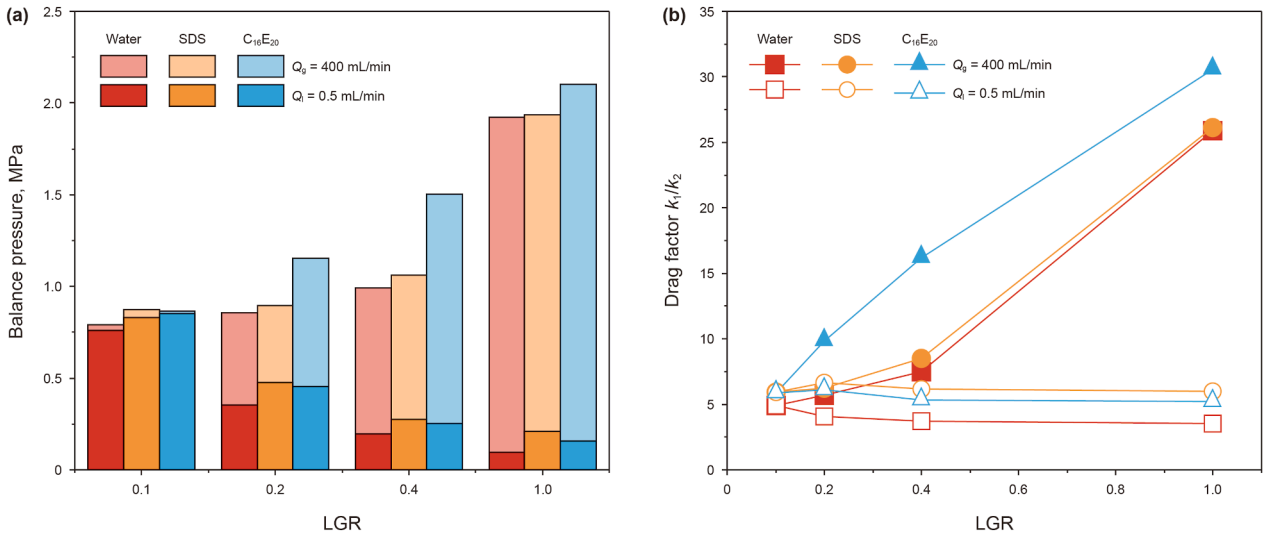

Fig. 9. Effect of varying LGR on balance pressure (**a**) and drag factor (**b**).

in liquid phase shearing the gas phase. In contrast, the 45° outlet exhibits superior adaptability to the simulated conditions, achieving more effective gas–liquid mixing. Therefore, given the consideration of both liquid intrusion into the outlet and the ease of liquid shearing of the CO_2, the outlet structure with a 45° downward inclination was selected.

In our previous work (Jiang et al., 2024), the diameters of gas and liquid chambers of the aerosol generator were also optimized. Table 1 shows the optimized structural parameters of the aerosol generator.

3.2. Preparation of aerosols with various interfacial properties

Introducing surfactants into the liquid phase allows for precise control over the gas–liquid interfacial properties and the stability of the generated aerosols. Two commercially utilized surfactants were selected for the experiment: the anionic surfactant SDS and the nonionic surfactant $C_{16}E_{20}$.

Both surfactants adsorb at the gas–liquid interface, forming molecular layers that prevent droplet coalescence and enhance aerosol stability, albeit through distinct mechanisms. $C_{16}E_{20}$ primarily relies on steric hindrance, its bulky hydrophilic polyoxyethylene chain forms a hydration layer, creating a physical barrier that prevents droplets from approaching and coalescing. In contrast, SDS imparts identical negative charges to the droplet surfaces, and the resulting electrostatic repulsion keeps them apart. Beyond stability, a key parameter influenced by surfactants is the interface modulus. This modulus quantifies the resistance of the interface to expansion and compression. A high interface modulus suppresses droplet deformation. When an aerosol droplet traverses a constrictive pore throat, it must deform, changing its interfacial curvature. This deformation induces an additional capillary resistance known as the Jamin effect. A high interfacial modulus enhances this resistance by stabilizing the deformation, thereby strengthening the blocking capacity of the aerosol and further reducing gas permeability.

The surface tension and interface modulus of the two surfactant solutions at different concentrations were measured (Figs. 6 and 7). The interface modulus initially increases and then decreases with surfactant concentration, peaking near the critical micelle concentration (CMC).

Based on the experimental results, the concentrations corresponding to the highest interfacial modulus values for the two surfactant solutions were selected. Specific details are listed in Table 2.

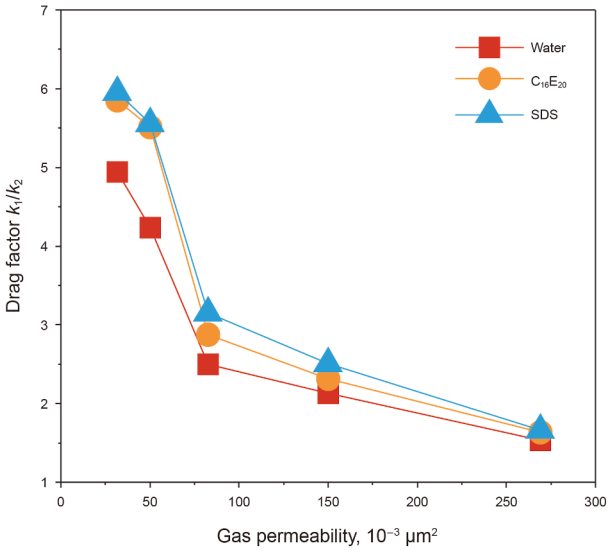

Fig. 12. Drag factor versus core gas permeability.

3.3. Factors affecting aerosol flow

3.3.1. LGR

Exploring LGR's impact on aerosols flow involved setting the core permeability at 31.59×10^{-3} μm², maintaining a gas flow rate of 400 mL/min, and altering the LGR by modifying the water flow rate. It should be noted that simulations spanned a broad LGR range to verify adequate mixing performance of the generator even under liquid-dominated conditions. However, in practical WAG field operations, as indicated in previous sections, LGR values generally remain close to 1. Accordingly, the LGR range was narrowed in the core flooding experiments to allow a more targeted investigation. Aerosols with different LGRs were injected into the core until the pressure stabilized. The alterations in pressure that ensued are depicted in Fig. 8. As the injection volume of aerosols

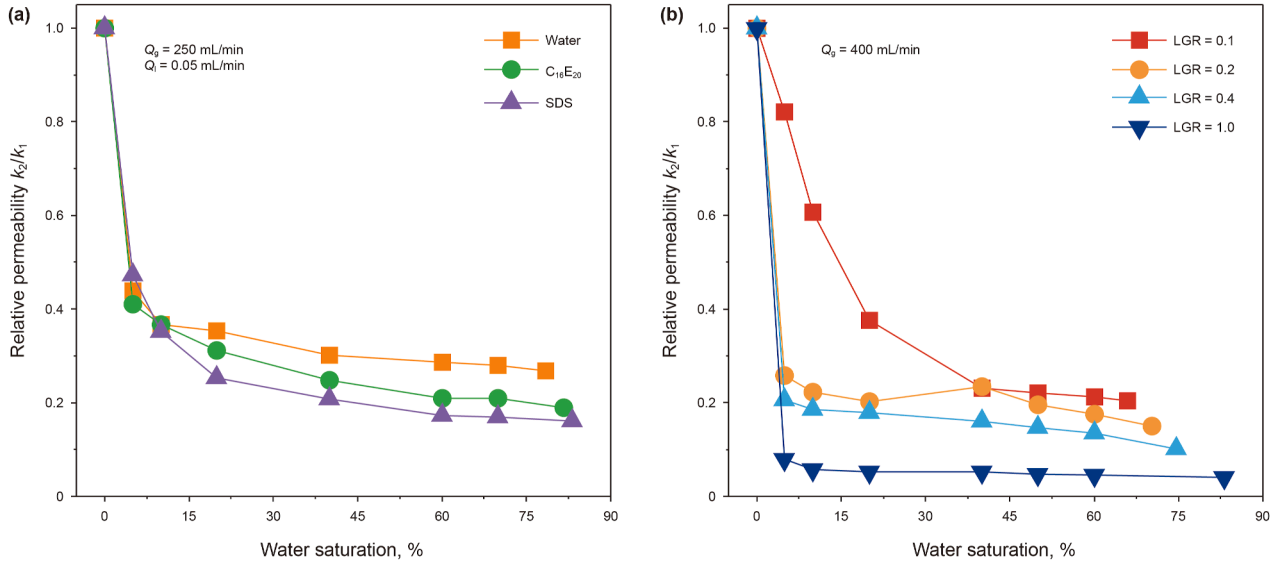

Fig. 13. Curves of gas relative permeability versus water saturation of the core during injection for different systems (**a**) and different LGR aerosols (**b**).

into the core rose, there was a swift increase in the injection pressure. Furthermore, when the LGR increased, the pressure required a longer time to reach equilibrium. For high LGR aerosols, significant fluctuations occurred even after the change in pressure has slowed down. This occurrence mirrors the Jamin effect. In addition, the continuous replacement of tiny liquid droplets within the core pores in the process of aerosol injection plays a role in the pressure fluctuations.

A comparative analysis was conducted on how different LGRs impact balance pressure and the drag factor of gas flow (Fig. 9), and the total mass flow rates corresponding to different LGRs were calculated (Fig. 10). Changes in both balance pressure and drag factor can be attributed to variations in the total mass flow rate. However, using balance pressure as an example, adjusting the LGR from 0.1 to 1.0 resulted in an average change rate of 135.72% when this target was achieved by adjusting the liquid flow. By contrast, when this was achieved by adjusting the CO_2 flow, the change rate of balance pressure was only 81.28%. Therefore, maintaining a steady gas flow rate allows for significant changes in aerosol injection pressure by modifying the liquid flow rate. Additionally, when contrasted with the water system, the aerosol created with a high interfacial modulus displayed a greater drag factor, attributed to its lower surface tension and enhanced interfacial viscoelasticity. The reduction in surface tension leads to a decrease in droplet size within aerosols, while the increase in interfacial modulus enhances droplet stability, thereby strengthening the Jamin effect generated within the pores.

To achieve a more accurate reflection of the influence of LGR on flow resistance, the total aerosol mass flow rate was fixed at 5.5 mg/s while varying LGR to investigate its effect on flow pressure. As depicted in Fig. 11, elevating the LGR leads to an increased balance pressure and drag factor, provided the total mass flow rate remains constant. This highlights the significant influence of liquid content on the resistance of aerosol flow. As a result, in aerosol injection processes, adjusting the liquid content enables straightforward control of injection pressure without requiring changes to the gas injection volume setup in the field.

3.3.2. Gas–liquid interface properties

As demonstrated in Figs. 9 and 10, a critical mass flow rate of approximately 6.0–9.0 mg/s was observed. In the lower flow rate range, the equilibrium pressure and resistance factor of the SDS system are greater than those of the $C_{16}E_{20}$ system. However, in the higher flow rate range, the reverse is true.

At elevated mass flow rates, droplet velocity and frequency of collision at pore throats increase (Jiang et al., 2024). Under these dynamic conditions, the higher interfacial modulus of the $C_{16}E_{20}$ system more effectively resists droplet deformation and compression, leading to a significantly stronger Jamin effect and consequently higher flow resistance compared to the SDS system. Conversely, at low total mass flow rates, droplets move slowly and have prolonged contact with pore surfaces. For the SDS system, the dominant electrostatic stabilization mechanism can be compromised. The adsorption of anionic SDS molecules onto the sandstone surface is postulated to weaken the inter-droplet electrostatic repulsion, promoting droplet coalescence and adsorption onto the rock. The resulting larger droplets can effectively bridge and block pore throats, forming stable plugs that are not easily displaced by the low-velocity gas flow.

3.3.3. Core permeability

An investigation into how core permeability affects the flow of aerosols within it was conducted, as depicted in Fig. 12. It was discovered that the link between permeability and pressure affects the drag factor, noting a steady decrease in the drag factor as the permeability increased. Significantly, the aerosols' capacity to control the gas markedly decreases when the permeability surpasses 100×10^{-3} μm^2.

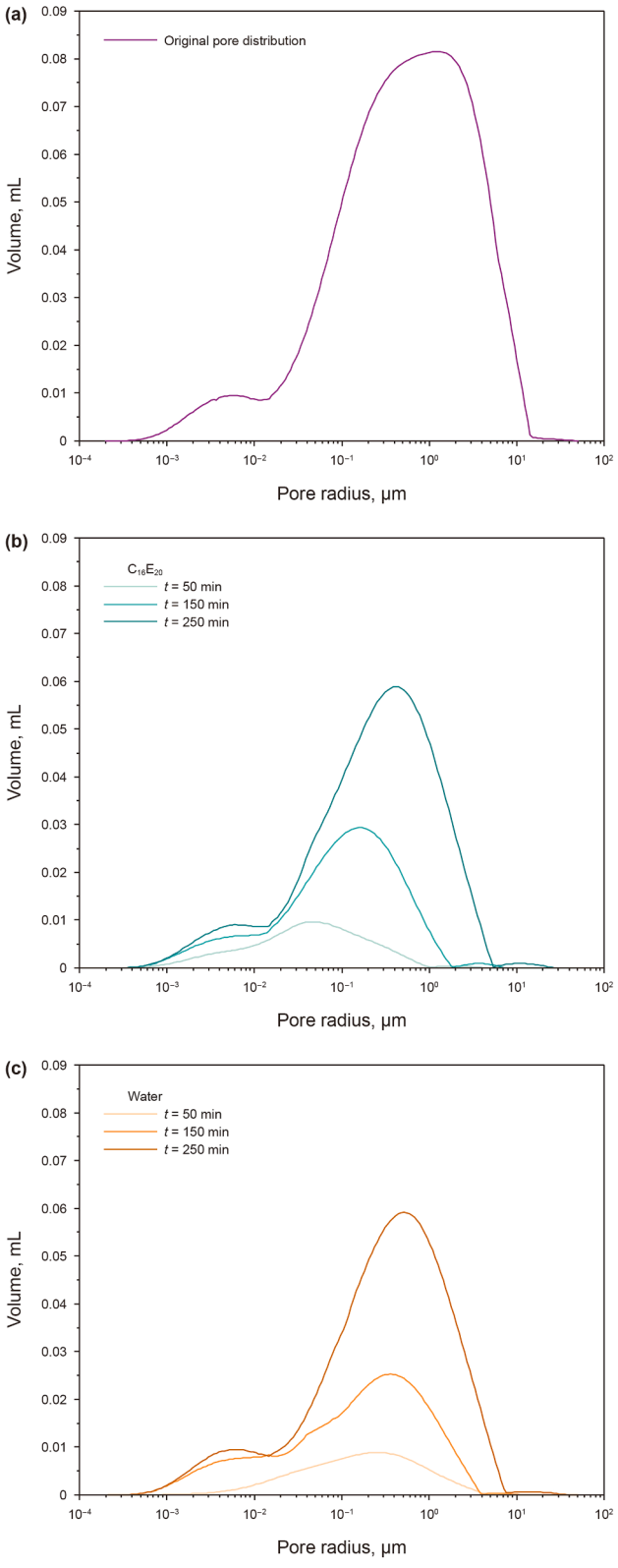

Fig. 14. (**a**) Original pore distribution curve of the core. Liquid phase distribution curves for $C_{16}E_{20}$ aerosol (**b**) and water aerosol (**c**) at different time points during the aerosol flooding.

Interfacial characteristics significantly affect flow resistance of aerosols, especially in cores with lower permeability, as shown by contrasting systems with different interfacial properties. Conversely, the variance in this drag effect becomes trivial when the permeability is higher. The main reason for this is the reduced spread of polydisperse aerosol systems in porous media and the lessened impact of interfacial properties on drag as the permeability and pore size increase.

3.3.4. Water saturation

The water saturation within the core was calculated based on the liquid phase flow rate and the pore volume of the core. The relationship between the relative permeability of gas and water saturation was analysed. Fig. 13(a) illustrates how various aerosol systems affect the gas permeability of the core when the aerosol injection parameters are the same. It is noticeable that with the rise in water saturation within the core, there is a notable reduction in relative permeability, especially in the initial stages of water saturation increase. Meanwhile, at high water saturations, the relative permeability is more sensitive to liquid phase composition. Systems with liquids that form viscoelastic interfaces exhibit stronger gas flow obstruction even at similar water saturations, owing to the stabilization of pore-blocking liquid architectures by the elastic interface.

Fig. 13(b) shows the relationship between water saturation and the relative permeability under different LGR conditions, maintaining a constant gas flow rate. It is evident that as the LGR rises, the rate of decrease in gas relative permeability accelerates. The aerosol injection rate is positively correlated with LGR. At low LGR, droplets are drawn into pores by capillary forces and distribute as films on pore surfaces. Gas flow paths remain relatively continuous and unobstructed, allowing gas flow to be gradually blocked as the water saturation increases. At high LGR, droplets collide violently at pore throats, increasing susceptibility to trapping. This phenomenon gives rise to the formation of bridge plugs or liquid rings, which rapidly impede the flow of gas through the pathway.

3.4. Distribution pattern of aerosols in cores

NMR was employed to characterize the distribution of the liquid phase at different time points during aerosol injection into the core. The permeability of the core sample is 81.55×10^{-3} μm^2. The original pore distribution curve, as measured by NMR, is illustrated in Fig. 14(a).

A comparison of the distribution pattern of the liquid phase in the core at different moments (Fig. 14) indicates that the aerosols greatly influence its distribution within the core in the first 50–150 min. Relative to the water system, The $C_{16}E_{20}$ system demonstrated a more limited range of initial saturated pore sizes, specifically between 0.04 and 0.21 μm. Conversely, the water system exhibited a more extensive range of 0.16–0.83 μm. The

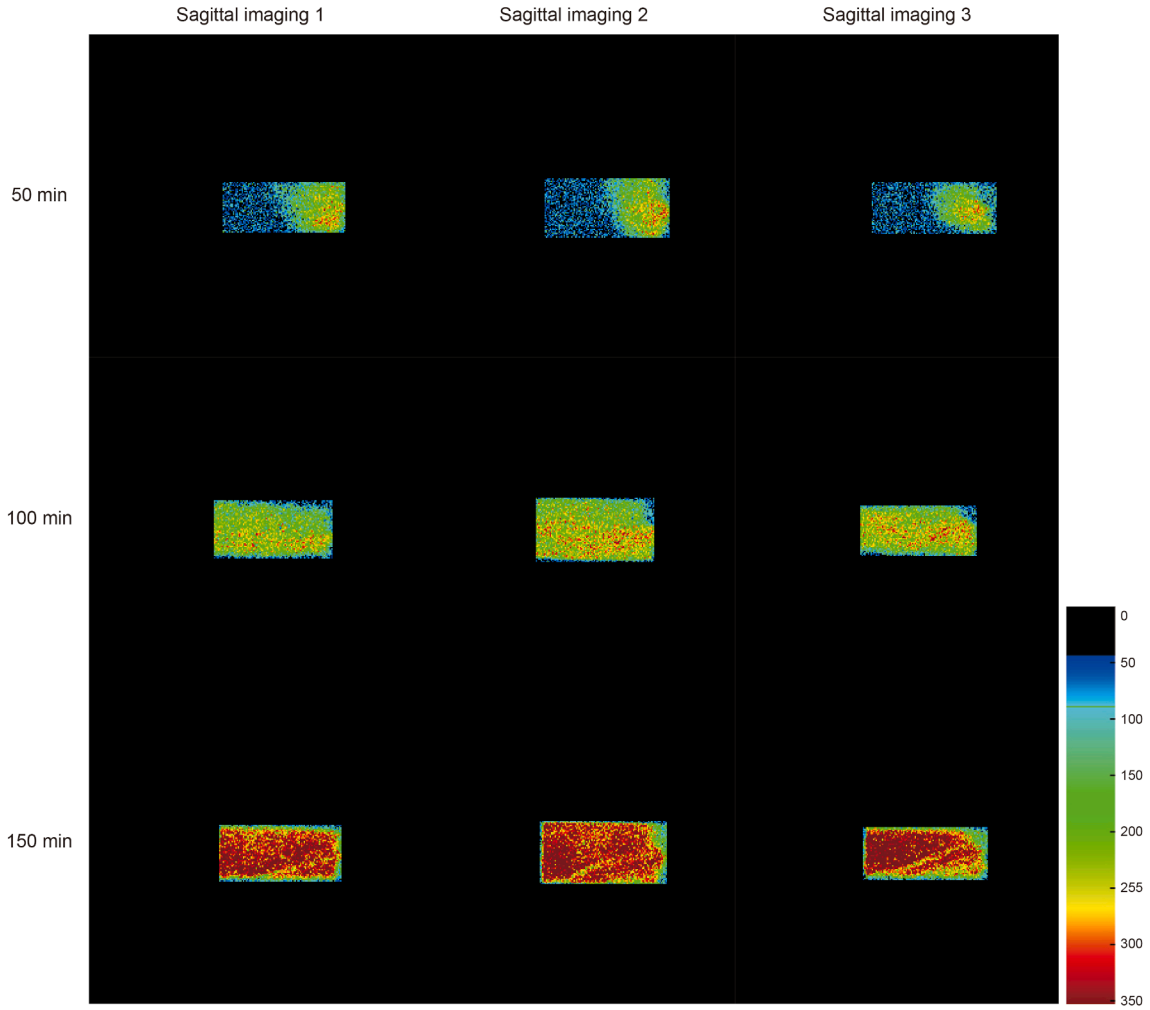

Fig. 15. Sagittal plane imaging for the core at different moments of flooding by water aerosol.

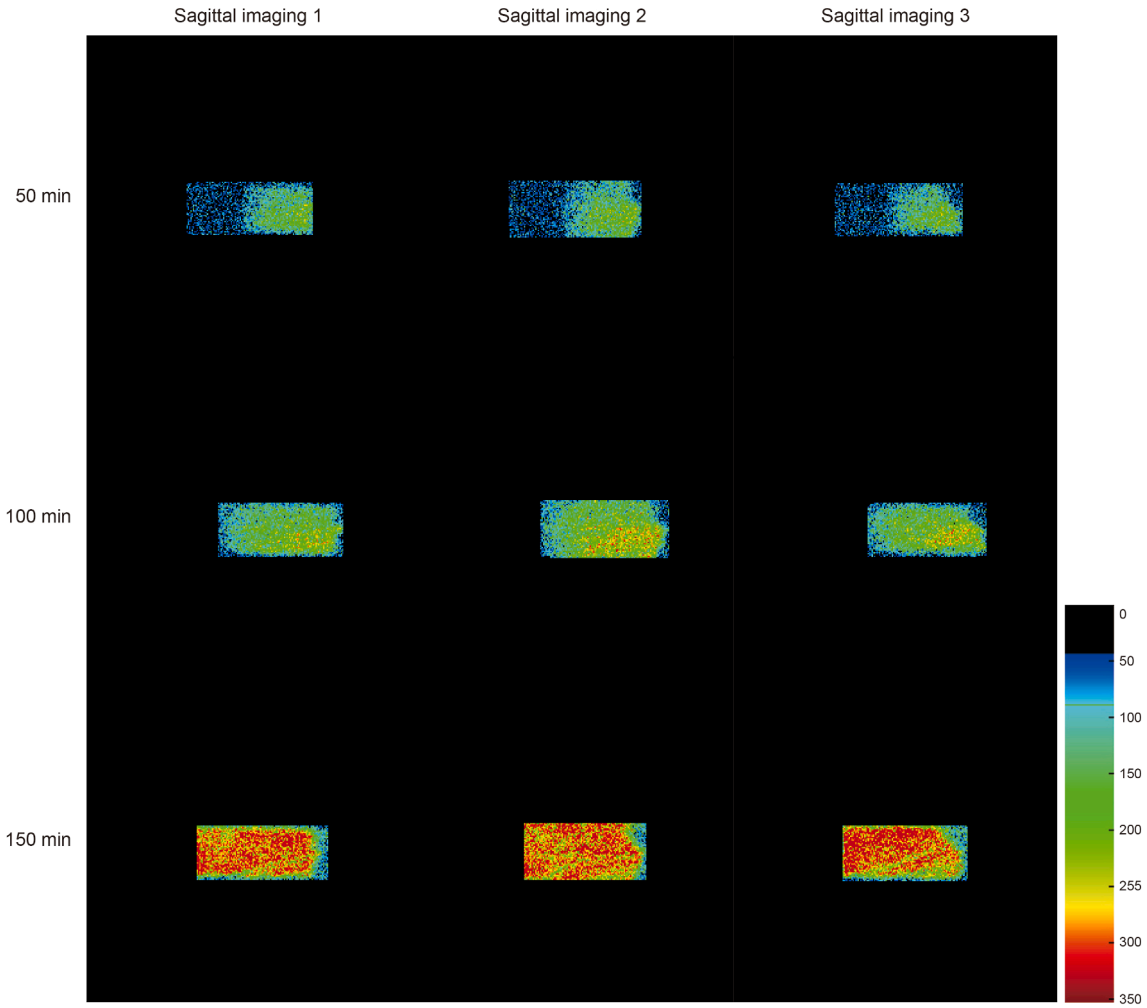

Fig. 16. Sagittal plane imaging for the core at different moments of flooding by $C_{16}E_{20}$ aerosol.

reason for this could be that in a surfactant aqueous phase, the system shows reduced surface tension, leading to the creation of droplets with smaller particles in the aerosol generator. Consequently, its ability to penetrate smaller pores is enhanced, resulting in higher saturation in these regions.

As illustrated in Fig. 15, sagittal scans of the core were conducted at various times during the process of water aerosol injection. As the process progresses for a duration of 50 min, a gradual accumulation of liquid phase was observed in the front half of the core, while the overall water saturation remained at a relatively low level. Following a duration of 150 min of injection, most pores in the core attain liquid saturation, thereby markedly enhancing the water saturation of the core. Water saturation reaches a stable state after 250 min.

Fig. 16 illustrates the sagittal imaging of the $C_{16}E_{20}$ system, revealing that within the first 50–150 min, the $C_{16}E_{20}$ aerosol markedly affects the distribution pattern of the liquid phase in the core. This contrasts with the simple water phase, where the $C_{16}E_{20}$ aerosol exhibits a much higher distribution in smaller pores than in the pure water-dispersed aerosol, enhancing dispersion stability. After 250 min, the distribution of both systems in the cores showed negligible variation.

The pressures of the two systems during the flooding were compared (see Fig. 17 and Table 3). The two pressure curves show similar patterns. However, during the initial phase (0–50 min) the injection pressure for water aerosol is higher. This phenomenon can be attributed to its propensity to enter large pores and obstruct the flow of CO_2. Furthermore, between 50 and 100 min, the injection pressure of $C_{16}E_{20}$ aerosol surpasses that of water aerosol.

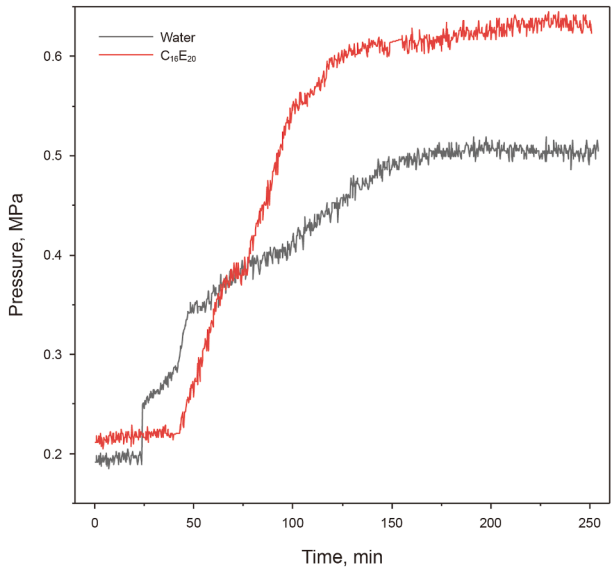

Fig. 17. Changes in injection pressure during displacement.

Table 3
Injected fluid volumes and corresponding injection pressures in cores at different injection stages.

Time, min	Injection liquid volume, mL		Injection pressure, MPa	
	Water aerosol	$C_{16}E_{20}$ aerosol	Water aerosol	$C_{16}E_{20}$ aerosol
50	0.504	0.506	0.341	0.257
150	1.503	1.503	0.491	0.614
250	3.312	3.239	0.507	0.636

This phenomenon can be attributed to the fact that water aerosol primarily blocks large pores, thereby allowing CO_2 to flow through small pores. Conversely, $C_{16}E_{20}$ aerosol preferentially seals small pores, resulting in comprehensive CO_2 blockage. After 150 min, there were fluctuations in pressure, but these were not significant overall. At this stage, the pressure difference between the two systems is primarily attributed to interfacial modulus, as the dominant flow resistance mechanism shifts from pore-throat access to the Jamin effect generated by droplet deformation during flow through the already filled pore network, which is significantly strengthened by the high interfacial modulus $C_{16}E_{20}$ droplets.

4. Conclusions

This study investigated the use of aerosols to mitigate gas channeling in CO_2 flooding, which adversely affects EOR and CO_2 geo-storage. The selection of an effervescent aerosol generator was made using the ANSYS simulation software, with the primary optimization of its gas outlet structure being the subsequent focus.

Core flooding experiments demonstrated that the liquid phase content is a critical factor influencing the flow resistance of aerosols. Significant increases in balance pressure and drag factor were observed when the LGR was raised under a constant total mass flow rate. Furthermore, adjusting the liquid flow rate enabled effective control of the injection pressure without altering the gas injection volume, providing operational flexibility for field applications. Additionally, it was found that the properties of the gas–liquid interface significantly influence the blocking capacity.

Core permeability exhibited a distinct threshold effect on the gas control capability of aerosols. The ability of aerosol to restrict gas flow diminished significantly when the permeability exceeded 100×10^{-3} μm^2. NMR imaging further revealed that $C_{16}E_{20}$-assisted aerosols preferentially entered smaller pores (0.04–0.21 μm), whereas pure water aerosols primarily occupied larger pores (0.16–0.83 μm). This indicates that the addition of surfactant enhanced the injectability and microscopic distribution uniformity of aerosols within low-permeability pores.

In summary, this study systematically investigates the flow characteristics and gas control mechanisms of aerosols in core across multiple levels. Subsequent work will include the characterization of fundamental aerosol properties, such as particle concentration and size distribution, to further validate the findings presented herein. Furthermore, experiments will be conducted on CO_2 flooding and oil displacement under high-temperature and high-pressure conditions, with a particular focus on investigating the flow behavior of aerosol systems when CO_2 reaches its supercritical state.

CRediT authorship contribution statement

Ping Jiang: Methodology, Funding acquisition, Conceptualization. **Chen-Xi Li:** Writing – review & editing, Writing – original draft, Visualization. **Kai Guo:** Validation, Methodology, Investigation, Conceptualization. **Gui-Cai Zhang:** Supervision, Methodology. **Ji-Jiang Ge:** Supervision, Methodology. **Ning Qi:** Resources, Methodology. **Yu-Kun Lu:** Resources.

Declaration of competing interest

The authors declare that they have no known competing financial interests or personal relationships that could have appeared to influence the work reported in this paper.

Acknowledgments

The authors acknowledge the financial support from the Natural Science Foundation of Shandong Province, China (ZR2020ME086).

References

Abdurrahman, M., Hidayat, F., Husna, U.Z., et al., 2021. Determination of optimum CO_2 water alternating gas (CO_2-WAG) ratio in Sumatera Light Oilfield. Mater. Today Proc. 39 (2), 970–974. https://doi.org/10.1016/j.matpr.2020.04.495.

Broniarz-Press, L., Ochowiak, M., Woziwodzki, S., 2010. Atomization of PEO aqueous solutions in effervescent atomizers. Int. J. Heat Fluid Flow 31 (4), 651–658. https://doi.org/10.1016/j.ijheatfluidflow.2010.02.005.

Chaturvedi, K.R., Ravilla, D., Kaleem, W., et al., 2021. Impact of low salinity water injection on CO_2 storage and oil recovery for improved CO_2 utilization. Chem. Eng. Sci. 229, 116127. https://doi.org/10.1016/j.ces.2020.116127.

Chen, J., Zhang, H., Wei, Q., et al., 2022. Mobility of water-soluble aerosol organic matters (WSAOMs) and their effects on soil colloid-mediated transport of heavy metal ions in saturated porous media. J. Hazard Mater. 440, 129733. https://doi.org/10.1016/j.jhazmat.2022.129733.

Chen, X., Zhang, Q., Trivedi, J., et al., 2024. Investigation on enhanced oil recovery and CO_2 storage efficiency of temperature-resistant CO_2 foam flooding. Fuel 364, 130870. https://doi.org/10.1016/j.fuel.2024.130870.

Cho, J., Min, B., Kwon, S., et al., 2021. Compositional modeling with formation damage to investigate the effects of CO_2–CH_4 water alternating gas (WAG) on performance of coupled enhanced oil recovery and geological carbon storage. J. Petrol. Sci. Eng. 205, 108795. https://doi.org/10.1016/j.petrol.2021.108795.

Choudhury, G., Tyagi, B., Singh, J., et al., 2019. Aerosol-orography-precipitation—A critical assessment. Atmos. Environ. 214, 116831. https://doi.org/10.1016/j.atmosenv.2019.116831.

da Silva, D.C., da Hora, L.F., de Araujo, J.D.C., et al., 2022. Evaluation of nonylphenol surfactant in enhanced oil recovery by SAG and WAG method. Fuel 314, 122717. https://doi.org/10.1016/j.fuel.2021.122717.

Dubovik, O., Li, Z., Mishchenko, M.I., et al., 2019. Polarimetric remote sensing of atmospheric aerosols: instruments, methodologies, results, and perspectives. J. Quant. Spectrosc. Radiat. Transf. 224, 474–511. https://doi.org/10.1016/j.jqsrt.2018.11.024.

Hall, R., Murdoch, L., Falta, R., et al., 2016. Evaluation of liquid aerosol transport through porous media. J. Contam. Hydrol. 190, 15–28. https://doi.org/10.1016/j.jconhyd.2016.03.003.

Hinds, W.C., Zhu, Y., 2022. Aerosol Technology: Properties, Behavior, and Measurement of Airborne Particles, third ed. Wiley, New York.

Jiang, P., Guo, K., Feng, K., et al., 2024. Influencing factors of aerosol system preparation by aerosol generator. J. China Univer. Petrol. (Edition of Natural Science) 48 (5), 146–150. https://doi.org/10.3969/j.issn.1673-5005.2024.05.016 (in Chinese).

Khan, M.Y., Kohata, A., Patel, H., et al., 2016. Water alternating gas WAG optimization using tapered WAG technique for a giant offshore Middle East Oil Fiel. In: Abu Dhabi International Petroleum Exhibition & Conference. https://doi.org/10.2118/183181-MS.

Kokhanovsky, A.A., 2013. Remote sensing of atmospheric aerosol using spaceborne optical observations. Earth Sci. Rev. 116, 95–108. https://doi.org/10.1016/j.earscirev.2012.10.008.

Kumar, S., Mandal, A., 2017. A comprehensive review on chemically enhanced water alternating gas/CO_2 (CEWAG) injection for enhanced oil recovery. J. Petrol. Sci. Eng. 157, 696–715. https://doi.org/10.1016/j.petrol.2017.07.066.

Lin, Z., Wang, Y., Zheng, F., et al., 2021. Rapid mass growth and enhanced light extinction of atmospheric aerosols during the heating season haze episodes in Beijing revealed by aerosol-chemistry-radiation-boundary layer interaction. Atmos. Chem. Phys. 21 (16), 12173–12187. https://doi.org/10.5194/acp-21-12173-2021.

Lv, L., Zhao, B., 2022. Deposition of non-spherical particles on indoor surfaces: Modification of diffusion coefficient. Aerosol. Sci. Technol. 56 (12), 1190–1200. https://doi.org/10.1080/02786826.2022.2134758.

Lwin, W.W., Srilaong, V., Boonyaritthongchai, P., et al., 2020. Electrostatic atomised water particles reduces postharvest lignification and maintain asparagus quality. Sci. Hortic. 271, 109487. https://doi.org/10.1016/j.scienta.2020.10948.

Ochowiak, M., Matuszak, M., Wlodarczak, S., et al., 2018. The concept design and study of twin-fluid effervescent atomizer with air stone aerator. Chem. Eng. Process. Process Intensif. 124, 24–28. https://doi.org/10.1016/j.cep.2017.11.020.

O'Sullivan, J.J., Norwood, E.-A., O'Mahony, J.A., 2019. Atomisation technologies used in spray drying in the dairy industry: A review. J. Food Eng. 243, 57–69. https://doi.org/10.1016/j.jfoodeng.2018.08.027.

Pöschl, U., 2005. Atmospheric aerosols: Composition, transformation, climate and health effects. Angew. Chem. Int. Ed. 44 (46), 7520–7540. https://doi.org/10.1002/anie.200501122.

Ren, B., Duncan, I.J., 2021. Maximizing oil production from water alternating gas (CO_2) injection into residual oil zones: The impact of oil saturation and heterogeneity. Energy 222, 119915. https://doi.org/10.1016/j.energy.2021.119915.

Roozbahani, A., Soofivand, F., Al-Tameemi, A.S.H., et al., 2024. A contrasting analysis of CO_2 and N_2 foam flood for enhanced oil recovery and geological storage of CO_2. Pet. Res. 9 (1), 55–60. https://doi.org/10.1016/j.ptlrs.2023.07.003.

Rostami, B., Fathollahi, A., Nejad, M.K., et al., 2026. Experimental study on parameter characterization of immiscible and near-miscible water-alternating-gas (WAG) injection using associated gas. Fuel 406, 137142. https://doi.org/10.1016/j.fuel.2025.137142.

Simjoo, M., Rezaei, T., Andrianov, A., et al., 2013. Foam stability in the presence of oil: Effect of surfactant concentration and oil type. Colloids Surf. A Physicochem. Eng. Asp. 438, 148–158. https://doi.org/10.1016/j.colsurfa.2013.05.062.

Spiteri, E.J., Juanes, R., 2006. Impact of relative permeability hysteresis on the numerical simulation of WAG injection. J. Pet. Sci. Eng. 50 (2), 115–139. https://doi.org/10.1016/j.petrol.2005.09.004.

Sun, C., Ning, Z., Qiao, X., et al., 2018. Measurements of internal flow regime and bubble size in effervescent atomizer. Exp. Therm. Fluid Sci. 98, 604–620. https://doi.org/10.1016/j.expthermflusci.2018.07.002.

Sun, X., Liu, J., Dai, X., et al., 2021. On the application of surfactant and water alternating gas (SAG/WAG) injection to improve oil recovery in tight reservoirs. Energy Rep. 7, 2452–2459. https://doi.org/10.1016/j.egyr.2021.04.034.

Vivek, R., Sivasankar, P., Kumar, G.S., 2017. Accelerating dissolution trapping by low saline WAG injection scenario. Energy Proc. 114, 5038–5047. https://doi.org/10.1016/j.egypro.2017.03.1655.

Wang, H., Guo, S., Wu, Z., et al., 2022. Secondary organic aerosol formation from straw burning using an oxidation flow reactor. J. Environ. Sci. 114, 249–258. https://doi.org/10.1016/j.jes.2021.08.049.

Wang, H., Kou, Z., Ji, Z., et al., 2023. Investigation of enhanced CO_2 storage in deep saline aquifers by WAG and brine extraction in the Minnelusa sandstone, Wyoming. Energy 265, 126379. https://doi.org/10.1016/j.energy.2022.126379.

Wang, X., Liu, C., Nie, J., et al., 2025. Microscopic seepage mechanism of nanofluids assistant CO_2 aerosol foam system flooding after water flooding. Fuel 384, 134049. https://doi.org/10.1016/j.fuel.2024.134049.

Wang, Y., Huerta, D.V., Kabir, C.S., et al., 2021. Immersive diagnostics of reservoirs under WAG injection, part I—Understanding the dynamics around the injector. J. Pet. Sci. Eng. 196, 1–16. https://doi.org/10.1016/j.petrol.2020.107829.

Wang, Z., Yang, S., Lei, H., et al., 2017. Oil recovery performance and permeability reduction mechanisms in miscible CO_2 water-alternative-gas (WAG) injection after continuous CO_2 injection: An experimental investigation and modeling approach. J. Pet. Sci. Eng. 150, 376–385. https://doi.org/10.1016/j.petrol.2016.11.003.

Wei, J., Zhou, X., Zhou, J., et al., 2021. Experimental and simulation investigations of carbon storage associated with CO_2 EOR in low-permeability reservoir. Int. J. Greenh. Gas Control 104, 103203. https://doi.org/10.1016/j.ijggc.2020.103203.

Yan, Y., Li, C., Dong, Z., et al., 2017. Enhanced oil recovery mechanism of CO_2 water-alternating-gas injection in silica nanochannel. Fuel 190, 253–259. https://doi.org/10.1016/j.fuel.2016.11.019.

Zhang, H., Gong, H., Wu, J., et al., 2024. Promoting dissolution behaviors of low-carbon alcohol polyoxyethylene polyoxypropylene ether in CO_2 by molecular structure optimization and adding cosolvent. J. Mol. Liq. 406, 125115. https://doi.org/10.1016/j.molliq.2024.125115.

Zhao, W., Huang, H., He, M., et al., 2025. Study on flame retardant effect and adsorption mechanism of ultrasonic atomized aerosol. Chem. Eng. Res. Des. 213, 296–308. https://doi.org/10.1016/j.cherd.2024.12.003.